Contents lists available at ScienceDirect

Electrochimica Acta

Heat generation in all-solid-state supercapacitors with graphene electrodes and gel electrolytes

Ampol Likitchatchawankun [a], Arpan Kundu [b], Obaidallah Munteshari [a, c],
Timothy S. Fisher [a], Laurent Pilon [a, *]

[a] Mechanical and Aerospace Engineering Department, Henry Samueli School of Engineering and Applied Science, University of California, Los Angeles, CA 90095, USA
[b] School of Mechanical Engineering and Birck Nanotechnology Center, Purdue University, West Lafayette, IN 47907, USA
[c] Mechanical Engineering Department, King Fahd University of Petroleum and Minerals (KFUPM), Dhahran, 31261, Saudi Arabia

A B S T R A C T

This study aims to investigate time-dependent heat generation in all-solid-state supercapacitors. Supercapacitors were fabricated by assembling two identical electrodes made of graphene petal arrays grown on buckypaper by microwave plasma chemical vapor deposition. The electrodes were separated by either (i) a conventional phosphoric acid in polyvinyl alcohol (PVA) gel electrolyte or (ii) a redox-active potassium ferricyanide/ferrocyanide in PVA gel electrolyte. The devices with redox-active gel electrolyte exhibited about three times larger capacitance due to additional charge storage by reversible redox reactions. However, their internal resistance was about six times greater than devices with conventional gel electrolyte due to the lower electrolyte ionic conductivity. The heat generation rate measured under constant-current cycling was the sum of irreversible and reversible contributions. The irreversible heat generation rate in all supercapacitors was caused by resistive losses, i.e., Joule heating. The reversible heat generation rate was different at the positive and negative electrodes and was affected by electric double layer (EDL) formation, reversible redox reactions, and/or the presence of negatively charged functional groups at the electrode surface. The results of this study can be used to gain insight into the charging mechanism and also to develop thermal management solution for all-solid-state supercapacitors.

© 2019 Elsevier Ltd. All rights reserved.

1. Introduction

In recent years, the overwhelming demand for portable consumer electronics and wearable devices has stimulated the need for lightweight, flexible, and reliable energy storage devices [1–4]. In this regard, all-solid-state supercapacitors are promising owing to their favorable properties such as low weight, manufacturing simplicity, and high power density [5–7]. All-solid-state supercapacitors are generally fabricated by sandwiching a piece of flexible gel electrolyte film between two flexible electrodes composed of carbon-based materials [8–10]. Pseudocapacitive materials such as transition metal oxides (e.g., RuO_2, MnO_2) [11–14] and conductive polymers [e.g., polyaniline (PANI), polypyrrole (PPy)] [15–18] have also been incorporated in the electrodes to induce pseudocapacitance.

Another interesting approach to increase the energy density and to enhance charge storage capacity of supercapacitor consists of adding redox species in the electrolyte. In such redox electrolyte systems, redox-active electrolytes and redox additive electrolytes are to be distinguished [19]. On the one hand, redox-active electrolytes consist solely of redox-active species, which can undergo electron transfer reactions [19]. On the other hand, redox additive electrolytes are mixture of non-redox electrolyte (e.g., KOH, H_2SO_4) and redox-active species [20]. The most common redox-active species include potassium iodide (KI) [21,22], potassium ferricyanide ($K_3Fe(CN)_6$) [23,24], sodium molybdate (Na_2MoO_4) [25], and hydroquinone [26,27], to name a few. Ion species present in these electrolytes undergo oxidation and reduction at the positive and negative electrodes during charging, thus producing pseudocapacitance and increasing capacitance [21,23,28]. For example, capacitance was reported to increase by 74% upon addition of KI [21] and by 212% with $K_3Fe(CN)_6$ [23] added to potassium hydroxide (KOH)

Nomenclature

A	Footprint area of the heat flux sensor, cm^2
C_{diff}	Differential capacitance, mF
C_{int}	Integral capacitance, mF
I	Current, mA
L	Electrode length, cm
m	Mass loading of active material in electrode, mg
n	Cycle number
q''	Heat flux, mW/cm^2
$\dot{Q}(t)$	Instantaneous heat generation rate, mW
$\overline{\dot{Q}}$	Time-averaged heat generation rate, mW
R_i	Resistance of electrode "i", Ω
R_s	Internal resistance of the cell, Ω
S	Entropy, J/K
S_i	Heat flux sensor sensitivity at electrode "i", μV/(W/cm^2)
t	Time, s

t_c^+, t_c^-	Time after or before the beginning of the discharging step, s
W	Electrode width, cm
ΔV	Voltage difference in the heat flux sensor, μV

Greek symbols

ν	Scan rate, mV/s
ψ_{min}, ψ_{max}	Minimum, maximum cell potential, V
$\psi_s(t)$	Cell potential, V

Superscripts and subscripts

c	Refers to charging step
cd	Refers to charging-discharging cycle
d	Refers to discharging step
J	Refers to Joule heating
T	Refers to entire cell
rev	Refers to reversible heat generation
$+$ or $-$	Refers to positive or negative electrode

in polyvinyl alcohol (PVA) gel electrolyte in supercapacitors with activated carbon electrodes. In general, reversible redox reactions occurring in the electrolyte may be exothermic or endothermic. In the specific case of ferricyanide/ferrocyanide redox pair, the redox reaction can be expressed as

$$Fe(CN)_6^{3-} + e^- \underset{oxidation}{\overset{reduction}{\rightleftharpoons}} Fe(CN)_6^{4-}. \tag{1}$$
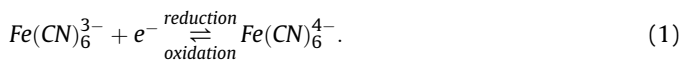
Here, the reduction reaction is exothermic while the oxidation is endothermic [29].

All-solid-state supercapacitor wearable electronic devices are in contact with the user. Thus, thermal management of these devices is vital to ensure comfort. Therefore, heat generation occurring within these devices must be quantified. To the best of our knowledge, the heat generation rate in all-solid-state supercapacitors has not been measured to date. The present study aims to extend our understanding of electrochemical processes through calorimetric measurements in all-solid-state supercapacitors with conventional gel or redox-active gel electrolytes consisting of carbon-based electrodes made of graphene petals grown on buckypaper (GP/BP). Measurements can also be used in the design of thermal management solutions.

2. Background

Several thermal models for supercapacitors have been proposed in the literature to predict the temperature evolution in commercial supercapacitors using analytical or numerical approaches. Many of these models solved the transient energy conservation equation with heat generation accounting solely for Joule heating [30–33]. By contrast, Schiffer et al. [34] developed a thermal model including reversible heat generation due to EDL formation and the associated changes in entropy of ions in the electrolyte. Indeed, the reversible heat generation rate was associated with changes in entropy of ions (entropy of mixing) [34]. During ion adsorption, ions migrated to the electrode/electrolyte interface to form the electric double layer. Then, the electrolyte system containing ions changes from a disordered to an ordered state and must lower its entropy S (i.e., $dS/dt < 0$). Under the isothermal conditions imposed by the calorimeter, the heat generation rate can be expressed as $\dot{Q}_{rev} = TdS/dt$. Thus, ion adsorption is an exothermic process, i.e., $\dot{Q}_{rev} < 0$. By

contrast, during ion desorption, ions redisperse into the bulk electrolyte such that the electrolyte system increases its entropy (i.e., $dS/dt > 0$) by absorbing thermal energy. Therefore, ion desorption is an endothermic process, i.e., with $\dot{Q}_{rev} > 0$ (see Supplementary Materials). In addition, the reversible heat generation rate was directly proportional to the imposed current [34].

More recently, d'Entremont and Pilon [35] developed a first-order time-dependent thermal analysis for EDLC devices based on the lumped-capacitance approximation and accounting for both Joule heating and reversible heat generation rate. The latter was modeled as proportional to the imposed current [35]. The predicted temperature evolution was in good agreement with experimental data obtained from commercial devices and reported in the literature [31,32,34]. The authors also developed a more sophisticated physical model based on first principles for coupled electrodiffusion, heat generation, and thermal transport in EDLCs [36,37] and hybrid supercapacitors [38]. For EDLCs, the energy conservation equation was derived and coupled with the modified Poisson-Nernst-Planck model (MPNP) for transient electrodiffusion in symmetric [36], or asymmetric [37] binary electrolytes. For both binary symmetric and asymmetric electrolytes, Joule heating was the only source of irreversible heat generation [36,37]. Reversible heat generation could be attributed to ion diffusion, steric effects, and entropy changes during charging and discharging [36]. The reversible heat generation rate was found to be exothermic during charging and endothermic during discharging [36]. For binary asymmetric electrolytes, reversible heat generation rates differed at the positive and negative electrodes [37]. The electrode with smaller counterion (ion with opposite charge to that electrode) and/or larger ion valency experienced stronger heat generation during galvanostatic cycling [37]. D'Entremont and Pilon [38] extended their model for EDLCs to hybrid pseudocapacitors by accounting for redox reactions and Li$^+$ intercalation in the pseudocapacitive electrode [38]. On the one hand, the irreversible heat generation originated from (i) Joule heating in the pseudocapacitive electrode and (ii) irreversible faradaic heat generation due to faradaic reactions in the Stern layer, and both were proportional to I^2 for small I [38]. On the other hand, the reversible heat generation rates originated from (i) EDL formation and (ii) faradaic reactions [38]. However, the time-averaged reversible heat generation rate due to EDL formation over a charging-discharging cycle was proportional to I^2 for small current I, whereas the time-averaged

reversible faradaic heat generation rate due to the faradaic reaction was equal to zero [38].

Few experimental studies have reported measurements of heat generation rates in electric double layer capacitors (EDLCs) [39–41]. Dandeville et al. [39] developed an electrochemical calorimeter to measure time-dependent temperature in (i) an EDLC cell consisting of two activated carbon electrodes and in (ii) a hybrid supercapacitor consisting of one activated carbon electrode and one MnO_2 electrode in an aqueous solution of 0.5 M K_2SO_4 under galvanostatic cycling. The heat generation rate was extracted by deconvolution of the measured temperature change in the cell during cycling [39]. Here, the heat generation rates at both electrodes of the EDLC cell were assumed to be identical so that the heat generation of each electrode was half that in the entire cell. Also, heat generation at the MnO_2 electrode in the hybrid cell was calculated by subtracting heat generation of one activated carbon electrode from the total heat generation rate in the entire hybrid supercapacitor [39]. The instantaneous heat generation rate in the cell was decomposed into (i) irreversible heat generation and (ii) reversible heat generation [39]. For activated carbon electrodes, the irreversible heat generation was found to be caused by Joule heating, whereas the reversible heat generation was found to be caused by electric double layer (EDL) formation [39]. By contrast, for an MnO_2 electrode, irreversible heat generation was found to be caused by Joule heating and irreversible faradaic heat generation, also called "polarization heat" [39], while reversible heat generation was found to be caused by redox reactions and EDL formation [39].

More recently, Munteshari et al. [40,41] developed an isothermal calorimeter to measure the instantaneous heat generation rates at each electrode of EDLC devices under constant current cycling. The cell tested consisted of two identical activated carbon electrodes with different liquid electrolytes [40] and electrode compositions [41]. Both irreversible and reversible heat generation rates were retrieved for each electrode [40,41]. Measurements first established that heat generation at each electrode may differ from one another [40]. The irreversible heat generation rate at both electrodes was proportional to I^2, where I is the imposed current [40]. Their sum was equal to Joule heating expressed as $\overline{Q}_J = R_s I^2$, where R_s is the internal resistance of the device. Reversible heat generation rate at the positive electrode was exothermic during charging and endothermic during discharging, as predicted theoretically [34,36]. Surprisingly, at the negative electrode, the reversible heat generation rate was both exothermic and endothermic during charging and discharging [40]. Asymmetry in the instantaneous heat generation rate between the positive and negative electrodes was shown to be caused by the presence of carboxymethyl cellulose (CMC) binder in the activated carbon electrodes [41]. In fact, after removing the CMC binder from the electrode constituents, the same heat generation rates were observed at the positive and negative AC-based electrodes [41]. The CMC binder consisted of carboxymethyl ($-CH_2COONa$) and hydroxyl ($-OH$) functional groups [41]. These groups dissociated in 1 M $LiPF_6$ in EC:DMC organic electrolyte forming negatively charged functional groups ($-CH_2COO^-$) and ($-O^-$) [41]. These negatively charged functional groups attracted cations, such as Li^+ ions, leading to overscreening of the electrode surface [41,42]. In order to charge-balance the inner Helmholtz layer in the electrolyte, another subsequent layer of anions was required [41,42]. Therefore, the negative electrodes with CMC was first charged by repelling this anion layer (endothermic) followed by cations adsorption (exothermic) [41,43]. By contrast, during charging, the positive electrode stored electrical energy by anion adsorption resulting in exothermic heat generation [41].

The present study aims to measure experimentally the instantaneous heat generation rate in all-solid-state supercapacitors with both conventional and redox-active gel electrolytes under galvanostatic cycling. It also aims to gain insights into the charge transport mechanisms as well as to quantify the heat generation for the design of the packaging to achieve adequate thermal comfort.

3. Materials and methods

3.1. Sample preparation

3.1.1. Electrode fabrication
Sheets of commercial buckypaper (Nanocomp Technologies, Inc., USA) with surface area 1.5×0.6 cm^2 were used as substrates to grow graphene petals (GPs) by microwave plasma chemical vapor deposition (MPCVD), as described in previous studies [44–46]. Buckypaper serves as a flexible, light, and mechanically robust substrate for GP growth. The buckypaper samples were elevated 9 mm above a 55 mm diameter molybdenum puck by ceramic spacers and then subjected to MPCVD conditions with H_2 (50 sccm, standard cubic centimeters per minute) and CH_4 (10 sccm) as the primary feed gases. During GP growth, the total pressure and plasma power were maintained at 30 Torr and 600 W, respectively. The growth time was 25 min. The mass loading of GPs on each electrode was measured by subtracting the weight of the original buckypaper (BP) (i.e., 1.96 mg/cm^2) from the final weight of each electrode.

3.1.2. Polymer gel electrolyte preparation
Two types of gel electrolytes were prepared: (i) 1 M H_3PO_4-PVA as a conventional gel electrolyte and (ii) 0.02 M $K_3Fe(CN)_6$-$K_4Fe(CN)_6$-PVA as a redox-active gel electrolyte. First, to prepare the PVA solution, 4 g of PVA powder (molecular weight 89,000–98,000 g/mol, 99%, hydrolyzed, Sigma-Aldrich) was dissolved in 40 ml of deionized water, and the resulting solution was subjected to continuous stirring for 20 min at 85 °C in a water bath.

For preparing H_3PO_4-PVA gel electrolyte, 4 g of concentrated liquid H_3PO_4 solution (85 wt% in H_2O, 99% trace metals basis, Sigma-Aldrich) was added to 40 ml of the previously prepared PVA solution. For synthesizing the redox-active gel electrolyte, $K_3Fe(CN)_6$-$K_4Fe(CN)_6$-PVA (denoted by PFC-PVA), 0.329 g of $K_3Fe(CN)_6$ powder (molecular weight 329.26 g/mol, 99%, Sigma-Aldrich) and 0.422 g of $K_4Fe(CN)_6$ powder (molecular weight 422.39 g/mol, 99%, Sigma-Aldrich) were dissolved in 10 ml DI water to prepare a 0.1 M $K_3Fe(CN)_6$/$K_4Fe(CN)_6$ solution (PFC solution). Then, the aqueous PFC solution was added to 40 ml of the previously prepared PVA solution to create 0.02 M PFC-PVA solution. For both gel electrolytes, 5 ml of the solutions were allowed to cool to room temperature. The resulting homogeneous viscous solution was drop-casted onto a polytetrafluoroethylene (PTFE) evaporating dish and allowed to dry at room temperature for 24 h. Finally, dried free-standing electrolyte films about 100 μm in thickness were cut into small pieces matching the size of the GP/BP electrodes.

3.1.3. Device assembly
To fabricate an all-solid-state supercapacitor, a clean paintbrush was dipped into the desired gel electrolyte solution and applied on two identical GP/BP electrodes. The electrodes were left to dry for about 45 min before the procedure was repeated twice. The objective of the initial coating and drying process was to achieve a complete coverage of the porous electrodes by the electrolyte and good adhesion between the electrode and the solid electrolyte film. After the third application, the device was assembled by sandwiching the gel electrolyte film between two identical GP/BP electrodes. Then, the device was placed between two glass

microscope slides of dimensions 2.5×7.5 cm^2 and pressure was applied with a small paper clip on each end of the slides. The assembled device was left at room temperature for 1 h prior to experimental measurements in order to evaporate the excess water.

Fig. S1 (see Supplementary Materials) illustrates the final appearance of the all-solid-state supercapacitor devices assembled in this study along with typical dimensions. Table 1 summarizes the composition of the gel electrolyte, length, width, and graphene (GP) mass loading of each electrode in the four devices assembled. The cross-sectional area and the thickness of Devices 2, 3, and 4 were identical and equal to (1.4×0.6 cm^2) while the cross-sectional area of Device 1 was slightly smaller (1.1×0.6 cm^2).

3.2. Isothermal calorimeter

In this study, instantaneous heat generation rates were measured in Devices 1 to 4 under galvanostatic cycling using a custom-made isothermal calorimeter previously described [40]. The calorimeter can measure the time-dependent heat generation rate in each electrode of an electrochemical cell separately with high accuracy ($\pm 10\,\mu$W) and with uncertainty under 3% [40]. Based on the thermal analysis of a single electrode described in supplementary material of Ref. [40], the time-dependent heat generation rate $\dot{Q}_i(t)$ (in mW) at each electrode is equal to the heat transfer rate $q_i''(t)$ passing through the heat flux sensor such that [40],

$$\dot{Q}_i(t) = q_i''(t)A_i = \frac{\Delta V_i(t)}{S_i}A_i \quad \text{with } i = + \text{ or } - \tag{2}$$

where A_i denotes the footprint area of the electrode (in cm^2) while S_i is the temperature-dependent sensitivity of the heat flux sensor provided by the manufacturer (in μV/(W/m^2)) while subscript "i" refers to either the positive "$+$" or negative "$-$" electrode. Here, $\Delta V_i(t)$ is the voltage difference measured in each heat flux sensor in thermal contact with electrode "i". The instantaneous total heat generation rate in the entire device (denoted by subscript "T") can be expressed as $\dot{Q}_T(t) = \dot{Q}_+(t) + \dot{Q}_-(t)$.

The instantaneous heat generation rate $\dot{Q}_i(t)$ can be decomposed as the sum of the irreversible $\dot{Q}_{irr,i}(t)$ and reversible heat generation rates $\dot{Q}_{rev,i}(t)$, i.e., $\dot{Q}_i(t) = \dot{Q}_{irr,i}(t) + \dot{Q}_{rev,i}(t)$ [40]. The time-averaged heat generation rate over a cycle period t_{cd} corresponds to the time-averaged irreversible heat generation rate $\overline{Q}_{irr,i}$ at electrode "i", i.e. [40],

$$\overline{Q}_{irr,i} = \frac{1}{t_{cd}} \int_{(n-1)t_{cd}}^{nt_{cd}} \dot{Q}_i(t)\, dt \quad \text{with } i = + \text{ or } - \tag{3}$$

where n is the cycle number, chosen to be adequately large so that $\dot{Q}_i(t)$ has reached oscillatory steady state. Indeed, by definition, time-averaging of the reversible heat generation rate $\dot{Q}_{rev,i}(t)$ at

electrode "i" over a complete charging-discharging cycle yields $\overline{\dot{Q}}_{rev,i} = 0$.

Finally, in the interest of comparing the reversible heat generation rate at each electrode, the instantaneous reversible heat generation rate $\dot{Q}_{rev,i}(t)$ was averaged over a charging period t_c of galvanostatic cycling [40],

$$\overline{\dot{Q}}_{rev,i}^c = \frac{1}{t_c} \int_{(n-1)t_{cd}}^{(n-1)t_{cd}+t_c} \dot{Q}_{rev,i}(t)\, dt \quad \text{with } i = T, +, \text{ or } - . \tag{4}$$

3.3. Device characterization

A device's integral capacitance C_{int} (in mF) was evaluated by integrating the area enclosed by the cyclic voltammetry (CV) curve plotting the measured current I (in mA) versus the imposed potential ψ_s (in V) for a given scan rate ν and potential window ranging between ψ_{min} and ψ_{max} as [47],

$$C_{int}(\nu) = \frac{1}{(\psi_{max} - \psi_{min})} \oint \frac{I}{2\nu}\, d\psi_s. \tag{5}$$

Here, the integral capacitances C_{int} of Devices 1 to 4 were obtained for scan rates 5, 10, 20, and 30 mV/s.

Subsequently, galvanostatic cycling was performed on each device, for 20 cycles at constant current I ranging from 1 to 4 mA to reach oscillatory steady state. Table 2 summarizes the conditions, namely the potential window ($\psi_{max} - \psi_{min}$) and current I for CV and galvanostatic cycling of each device. The potential window for both CV and galvanostatic cycling was 1.0 V for Device 1, 0.8 V for Device 2, and 1.2 V for Devices 3 and 4. These potential windows were chosen during CV pre-cycling of each device in order to avoid unwanted redox reactions.

Moreover, the internal resistance R_s was evaluated from the IR drop at the charging/discharging transitions under galvanostatic cycling at current I according to Refs. [48—51],

$$R_s(I) = \frac{\psi_s(t_c^+) - \psi_s(t_c^-)}{2I} \tag{6}$$

where $\psi_s(t_c^+)$ and $\psi_s(t_c^-)$ denote the potential across the device at

Table 2
Cyclic voltammetry and galvanostatic cycling operating conditions for four devices.

Device	Cyclic Voltammetry (CV)	Galvanostatic cycling	
	Potential window	Current imposed	Potential window
	ψ_{min} - ψ_{max}	I (mA)	ψ_{min} - ψ_{max}
1	0—1.0 V	2.0—4.0	0—1.0 V
2	0—0.8 V	1.0—4.0	0—0.8 V
3	0—1.2 V	1.0—4.0	0—1.2 V
4	0—1.2 V	1.0—4.0	0—1.2 V

Table 1
Gel electrolyte composition, footprint and mass loading of graphene petals (GP) on buckypaper for the four devices investigated.

Device	Gel electrolyte	Footprint	Mass loading of GP electrodes	
		L $\times$ W	positive	negative
1	1 M H$_3$PO$_4$-PVA	1.1 cm $\times$ 0.6 cm	3.98 mg	3.06 mg
2	1 M H$_3$PO$_4$-PVA	1.4 cm $\times$ 0.6 cm	3.85 mg	4.53 mg
3	0.02 M K$_3$Fe(CN)$_6$-K$_4$Fe(CN)$_6$-PVA	1.4 cm $\times$ 0.6 cm	4.55 mg	3.83 mg
4	0.02 M K$_3$Fe(CN)$_6$-K$_4$Fe(CN)$_6$-PVA	1.4 cm $\times$ 0.6 cm	2.65 mg	2.87 mg

the end of the charging step and immediately after the beginning of the discharging step, respectively. Here, the IR drop $[\psi_s(t_c^+) - \psi_s(t_c^-)]$ was calculated by considering the cell potential $\psi_s(t_c^-)$ 10 ms after the beginning of the discharging step (i.e. $t_c^- - t_c^+ = 10$ ms), as suggested by Zhao et al. [49].

4. Results and discussion

4.1. Cyclic voltammetry curves and integral capacitances

Fig. 1 shows the CV curves at scan rates $\nu = 5, 10, 20$, and 30 mV/s measured for Devices 1 to 4 under the operating conditions listed in Table 2. The nearly rectangular CV curves of Devices 1 and 2 featuring conventional gel electrolyte are characteristic of EDLCs behavior. By contrast, Devices 3 and 4 with redox-active gel electrolyte exhibited CV curves with peaks attributed to reversible redox reactions. Here, the redox peaks were observed in the potential range $\psi_s(t) \sim 0-0.4$ V corresponding to the faradaic regime when charging was dominated by redox reactions [52].

Fig. 2 plots the integral capacitance C_{int}, estimated from CV curves using Equation (5), for all four devices as a function of scan rate ν. As expected, the integral capacitance C_{int} of Devices 3 and 4 with redox-active gel electrolyte was about two to three times larger than that of Device 2 with conventional gel electrolyte for the same footprint area, albeit with slightly larger potential windows. This result can be attributed to additional charge storage due to redox reactions in the redox-active gel electrolyte of $Fe(CN)_6^{3-}/Fe(CN)_6^{4-}$ redox pair. This improvement in C_{int} has also been observed for different redox electrolytes [21–27], as previously discussed. In addition, Fig. 2 indicates that the integral capacitances C_{int} of all devices decreases with increasing scan rate. The slight decrease of C_{int} in Devices 1 and 2 is consistent with results for EDLC devices with activated carbon electrodes reported in Ref. [40]. However, the decrease in C_{int} for Devices 3 and 4 was steeper than for Devices 1 and 2. This observation is consistent with results for graphene-based solid-state flexible supercapacitor using polymer gel electrolyte with sodium molybdate (Na_2MoO_4) as a redox additive electrolyte [53]. This observation can be attributed to the slow kinetics of the faradaic reactions in redox-active electrolytes, producing less total charge storage at higher scan rates. In addition, Devices 1 to 4 showed either better or comparable capacitance comparing to some other all-solid-state supercapacitor devices reported in Refs. [7,54,55], as shown in Table S1 in Supplementary Materials.
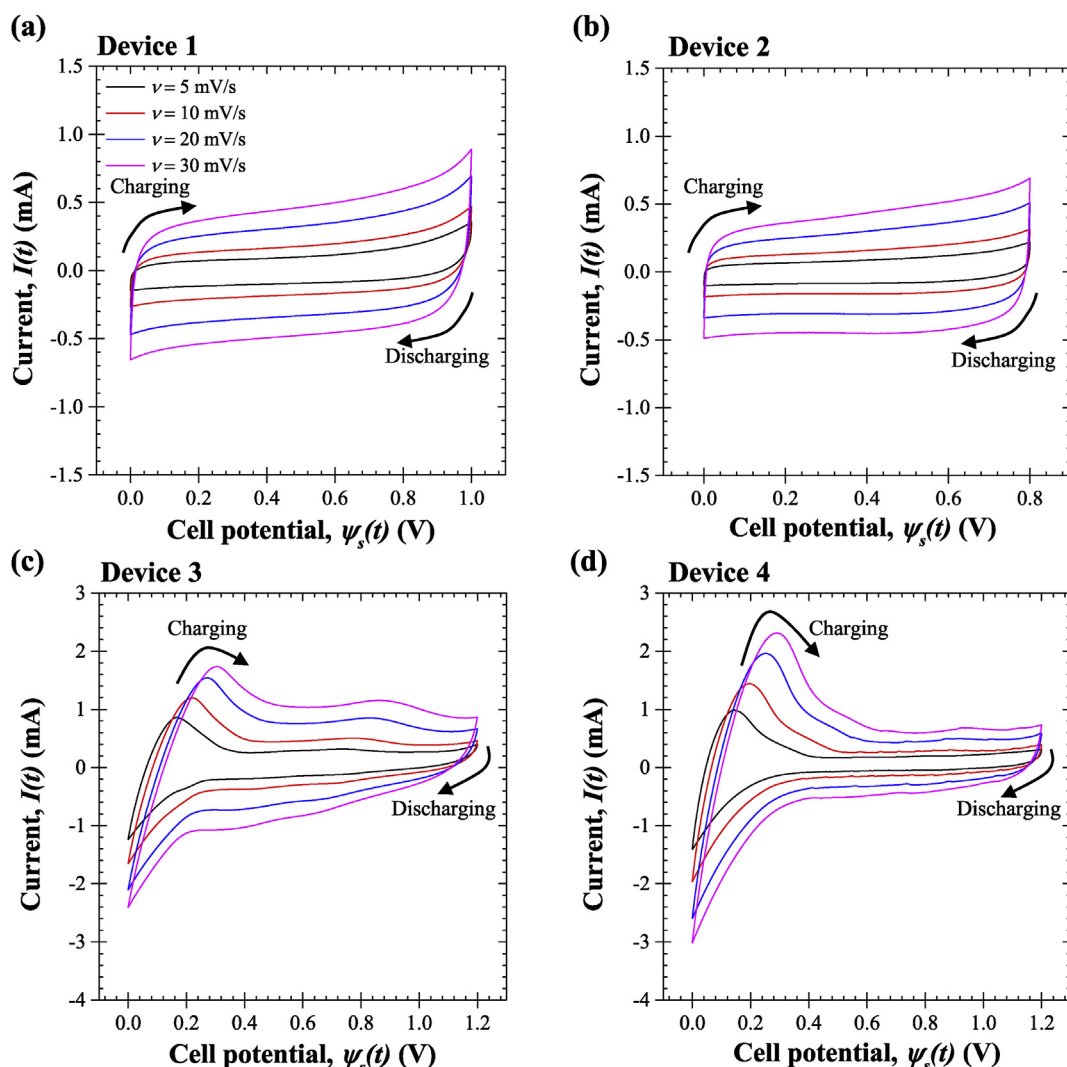
Fig. 1. Cyclic Voltammetry (CV) curves for (a) Device 1, (b) Device 2, (c) Device 3, and (d) Device 4 for scan rate $\nu = 5, 10, 20$, and 30 mV/s for different potential windows (Table 2).
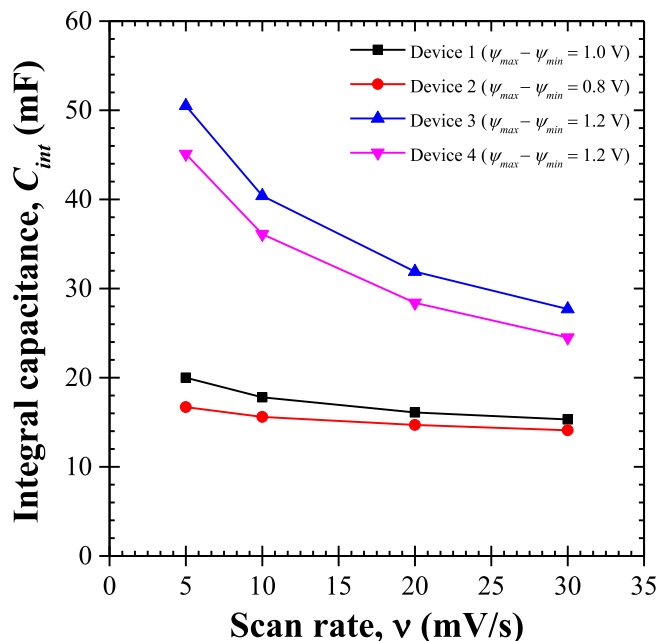
Fig. 2. Integral capacitance $C_{int}(\nu)$ obtained from CV curves [Equation (5)] presented in Fig. 1 for the four devices investigated as a function of scan rate ν for $\nu = 5$, 10, 20, and 30 mV/s.

4.2. Galvanostatic cycling and internal resistances

Fig. 3 shows the cell potential $\psi_s(t)$ as a function of time t during galvanostatic cycling of Devices 1 to 4 for constant current I ranging from 1 to 4 mA and the same potential windows as for the CV curves (see Fig. 1). For Devices 1 and 2 [Fig. 3(a) and (b)], the cell potential $\psi_s(t)$ varies linearly with time t between the minimum ψ_{min} and maximum ψ_{max} potentials. This result confirms the EDLC behavior of Devices 1 and 2 and the absence of redox reactions. By contrast, for Devices 3 and 4 [Fig. 3(c) and (d)] the cell potential $\psi_s(t)$ during galvanostatic cycling did not vary linearly with time t. The cell potential $\psi_s(t)$ features a small slope at the beginning of charging indicating larger differential capacitance $C_{diff} = I/(d\psi_s/dt)$ [56] at the early stage of the charging process from $\psi_s(t) \sim 0-0.4$ V. This potential range corresponded to the faradaic regime when faradaic reactions dominated [57] (see Fig. S3 in Supplementary Materials). This interpretation is consistent with observation of the redox peaks in CV curves (Fig. 1). The larger differential capacitance C_{diff} can be attributed to faradaic reactions (faradaic regime) during charging, while the smaller differential capacitance C_{diff} in the second part of the charging process (capacitive regime) from $\psi_s(t) \sim 0.4-1.2$ V, can be attributed to EDL formation [57]. Moreover, in all devices, IR drop $[\psi_s(t_c^+) - \psi_s(t_c^-)]$ can be observed at the transition between the end of charging and the beginning of discharging.

Fig. 4 shows the associated internal resistance R_s of Devices 1 to 4, calculated according to Equation (6), as a function of imposed current I. The internal resistance R_s in all four devices was fairly constant regardless of imposed current. However, the internal resistances R_s of Devices 3 and 4 with redox-active gel electrolyte were about five to six times larger than those of Devices 1 and 2. This observation can be attributed to the smaller ionic conductivity of redox-active gel electrolyte due to the much smaller ion concentration (0.02 M PFC-PVA), limited by the solubility of the salts, compared with the ion concentration of the conventional gel electrolyte (1 M H$_3$PO$_4$-PVA). Indeed, the ionic conductivity of

0.02 M PFC-PVA gel electrolyte has been reported as 6 mS cm^{-1} by Yang et al. [58] and 5.44 mS cm^{-1} by Kundu et al. [59]. On the other hand, the ionic conductivity of 1 M (1:1) H$_3$PO$_4$-PVA gel electrolyte has been reported to be larger than 10 mS cm^{-1} [60]. In addition, the internal resistance of Device 1 was about two times larger than that of Device 2. This observation seems counterintuitive given the fact that mass loading of the negative electrode of Device 2 was about 48% larger than that of Device 1. The larger resistance of Device 1 can be attributed to (i) variations in the drop-casting of the gel electrolyte that may have resulted in larger electrolyte thickness and/or (ii) variations in the device fabrication process due to poorer wetting and lower coverage of the electrode surface by the gel electrolyte. The latter would lead to poor electrical contact between the electrode and the viscous polymer gel electrolyte [20].

4.3. Instantaneous heat generation rates

Fig. 5 shows the temporal evolution of the measured heat generation rates (i) $\dot{Q}_-(t)$ at the negative electrode, (ii) $\dot{Q}_+(t)$ at the positive electrode, and (iii) $\dot{Q}_T(t) = \dot{Q}_+(t) + \dot{Q}_-(t)$ in the entire cell for Devices 1 to 4 as functions of dimensionless time t/t_{cd} for five consecutive galvanostatic cycles under constant current $I = 3$ mA. The results indicate that the heat generation rates in all four devices were repeatable over five consecutive cycles. Note such repeatability is not expected over hundreds or thousands of cycles as the device degrades. However, while the cyclic stability of the redox electrolyte device and its effect on heat generation is certainly important, it falls beyond the scope of the present study. In addition, the heat generation rates $\dot{Q}_-(t)$, $\dot{Q}_+(t)$, and $\dot{Q}_T(t)$ in Devices 3 and 4 were significantly larger than those in Devices 1 and 2 due, in part, to their larger internal resistance R_s (Fig. 4).

Moreover, $\dot{Q}_-(t)$, $\dot{Q}_+(t)$, and $\dot{Q}_T(t)$ in Device 1 was systematically larger than in Device 2 despite having similar capacitances because Device 1 had a larger internal resistance R_s and was cycled over a larger potential window (ψ_{max} - ψ_{min}) compared to Device 2. Furthermore, in both Devices 1 and 2, the heat generation rate at the positive electrode $\dot{Q}_+(t)$ was slightly larger than that at the negative electrode $\dot{Q}_-(t)$. This asymmetry in the heat generation rate at the positive and negative electrodes can be attributed to differences in charging mechanisms between the electrodes due to overscreening effect caused by negatively charged functional group on graphene electrodes, as observed also in activated carbon electrodes with CMC binder [41].

Finally, despite having the same electrode and electrolyte compositions, and similar capacitance and internal resistance, the heat generation rates $\dot{Q}_-(t)$ and $\dot{Q}_+(t)$ were significantly different in Devices 3 and 4 due to larger mass loading of GPs on the positive and negative electrodes of Device 3 than those of Device 4. The larger electrode/electrolyte interfacial area for charge storage produces higher heat generation rate.

4.4. Time-averaged heat generation rates

Fig. 5 shows the time-averaged irreversible heat generation rates (i) $\overline{\dot{Q}}_{irr,-}$ at the negative electrode, (ii) $\overline{\dot{Q}}_{irr,+}$ at the positive electrode, and (iii) $\overline{\dot{Q}}_{irr,T} = \overline{\dot{Q}}_{irr,-} + \overline{\dot{Q}}_{irr,+}$ in the entire cell, represented by dashed lines. The time-averaged irreversible total heat generation rate $\overline{\dot{Q}}_{irr,T}$ in Device 1 was larger than in Device 2 due to its larger internal resistance R_s (Fig. 4), as previously discussed. On the other hand, despite differences in the instantaneous heat generation rates, the time-averaged total heat generation rate $\overline{\dot{Q}}_{irr,T}$ was similar in Devices 3 and 4 as their internal resistance R_s was
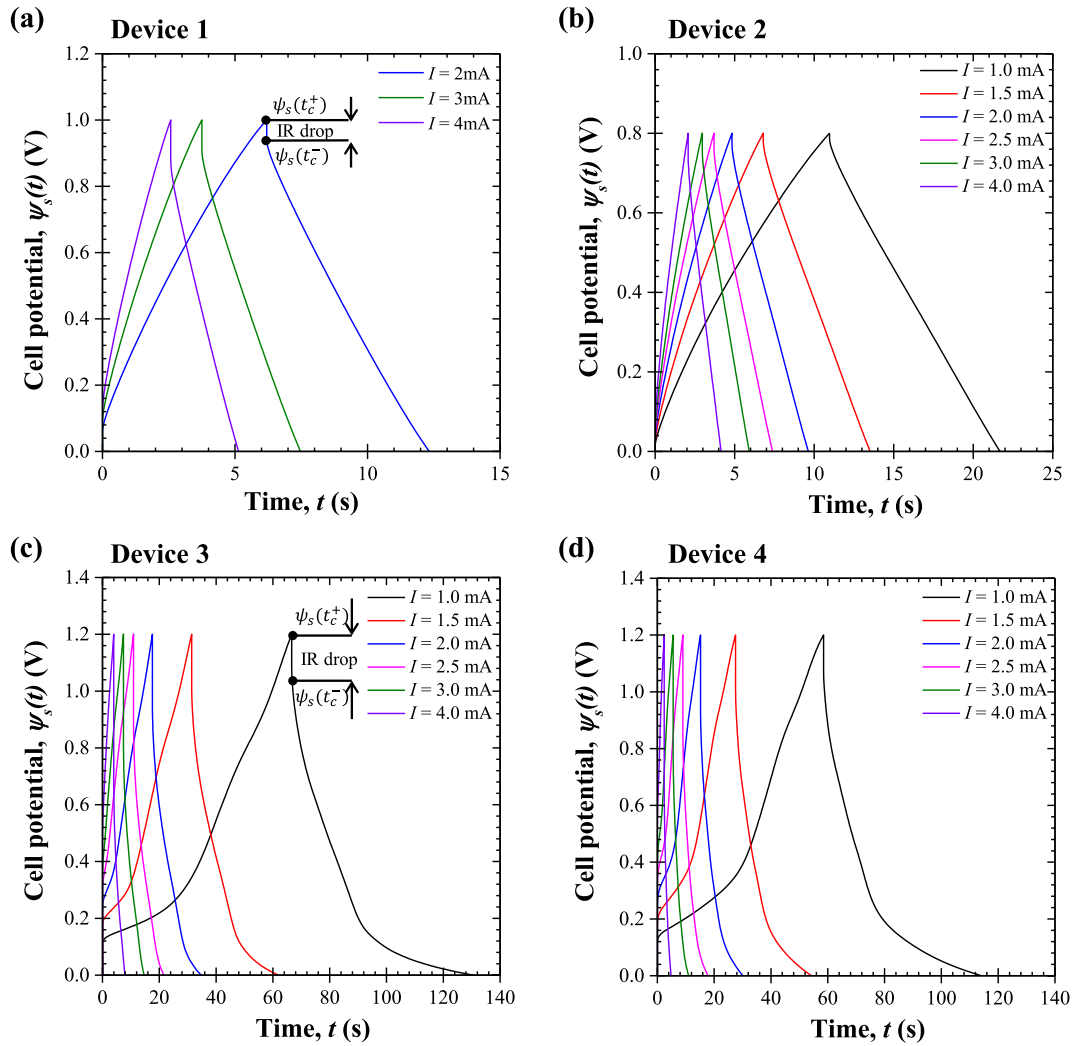
Fig. 3. Cell potential under galvanostatic cycling for (a) Device 1, (b) Device 2, (c) Device 3, and (d) Device 4 under imposed current I between 1 and 4 mA for different potential windows (Table 2).
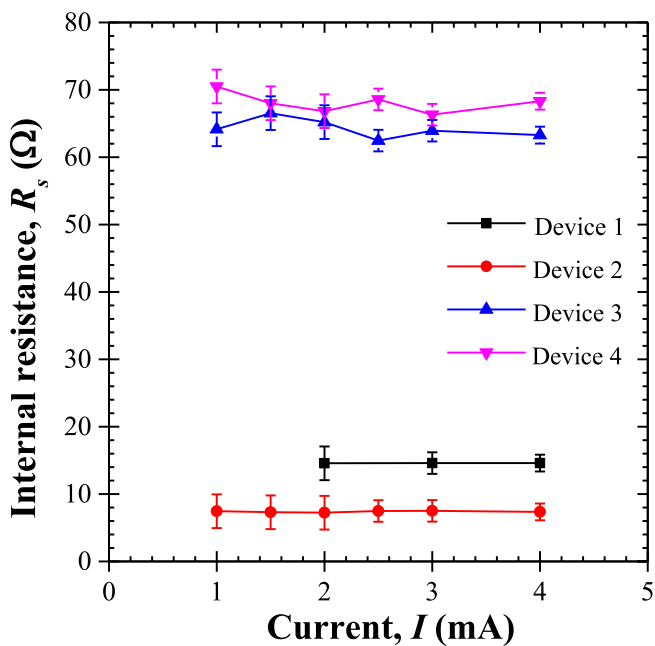
Fig. 4. Internal resistance R_s as a function of imposed current I for Devices 1 to 4 determined from Equation (6) based on the IR drop shown in Fig. 3.

comparable (Fig. 4).

Fig. 6 plots the time-averaged irreversible heat generation rates $\overline{\dot{Q}}_{irr,-}$, $\overline{\dot{Q}}_{irr,+}$, and $\overline{\dot{Q}}_{irr,T}$ as functions of I^2 for Devices 1 to 4 under constant current cycling. It also shows the heat generation rate due to Joule heating expressed as $\overline{\dot{Q}}_J = R_s I^2$, where R_s is the average internal resistance for each device obtained from the IR drop (Fig. 4). The measured total irreversible heat generation rate $\overline{\dot{Q}}_{irr,T}$ under galvanostatic cycling was in excellent agreement with Joule heating $\overline{\dot{Q}}_J = R_s I^2$ for all four devices considered. In other words, Joule heating was the only cause of irreversible heat generation in the all-solid-state supercapacitors considered, including those with redox-active gel electrolytes. In addition, the time-averaged heat generation rates $\overline{\dot{Q}}_{irr,-}$ and $\overline{\dot{Q}}_{irr,+}$ at the negative and positive electrodes were also linearly proportional to I^2, and the coefficient of proportionality corresponded to their respective resistances R_- and R_+. In fact, for all four devices tested, Fig. 6 indicates that the two electrodes had similar resistances whose sum corresponds to the device internal resistance, i.e., $R_- \approx R_+$ and $R_- + R_+ \approx R_s$. Similar results were obtained previously with EDLCs with activated carbon electrodes of various compositions and with different electrolytes [40,41].

(a)

(b)

(c)

(d)
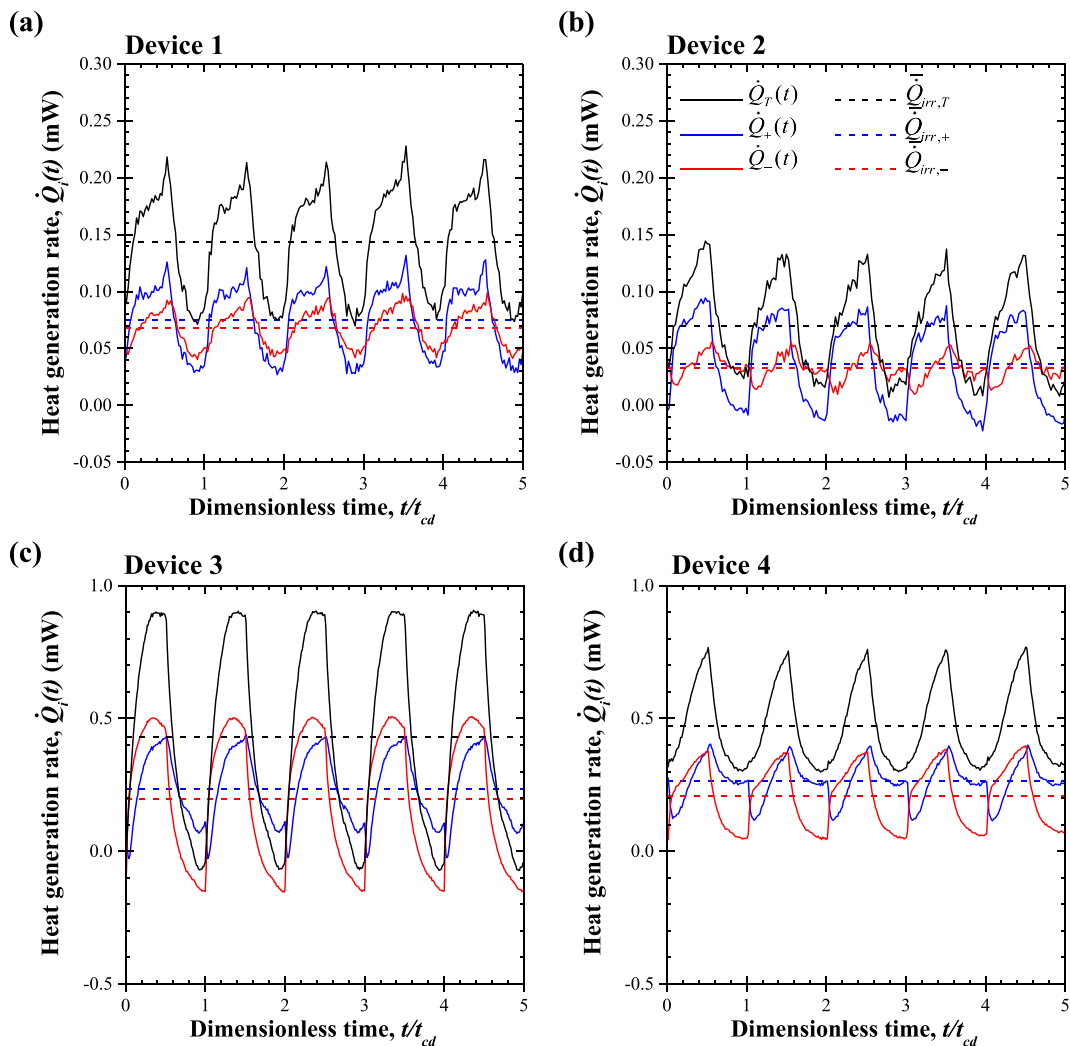
Fig. 5. Instantaneous heat generation rates $\dot{Q}_+(t)$, $\dot{Q}_-(t)$, and $\dot{Q}_T(t)$ and their time-averaged heat generation rates $\overline{\dot{Q}}_{irr,+}$, $\overline{\dot{Q}}_{irr,-}$, and $\overline{\dot{Q}}_{irr,T}$ at the positive and negative electrodes and for the entire cell for (a) Device 1, (b) Device 2, (c) Device 3, and (d) Device 4 under constant current cycling at $I = 3$ mA for potential windows (ψ_{max} - ψ_{min}) of 1.0 V, 0.8 V, 1.2 V, and 1.2 V, respectively (see Table 2).

4.5. Reversible heat generation rates

4.5.1. Conventional gel electrolyte

As previously demonstrated, Joule heating is the sole cause of irreversible heat generation. Thus, under constant current cycling, the instantaneous irreversible heat generation rate $\dot{Q}_{irr,i}(t)$ remains time-independent so that $\dot{Q}_{irr,i}(t) = \overline{\dot{Q}}_{irr,i} = R_i I^2$. Therefore, the instantaneous reversible heat generation rate $\dot{Q}_{rev,i}(t)$ at each electrode or in the entire device can be calculated by subtracting the time-averaged irreversible heat generation rate $\overline{\dot{Q}}_{irr,i}$ from the instantaneous heat generation rate $\dot{Q}_i(t)$, i.e.,

$$\dot{Q}_{rev,i}(t) = \dot{Q}_i(t) - \overline{\dot{Q}}_{irr,i} \quad \text{with } i = -, +, \text{ or } T. \quad (7)$$

Fig. 7 shows the instantaneous reversible heat generation rates (a) $\dot{Q}_{rev,+}(t)$ at the positive electrode, (b) $\dot{Q}_{rev,-}(t)$ at the negative electrode, and (c) $\dot{Q}_{rev,T}(t)$ in the entire cell estimated by Equation (7) for Devices 1 and 2 for current I ranging from 2 to 4 mA. The reversible heat generation rate at the positive electrode $\dot{Q}_{rev,+}(t)$ was systematically larger than that at the negative electrode

$\dot{Q}_{rev,-}(t)$ for both Devices 1 and 2 and at all imposed current I. At the positive electrode [Fig. 7(a)], the reversible heat generation rate $\dot{Q}_{rev,+}(t)$ was exothermic during charging and endothermic during discharging for both Devices 1 and 2. Moreover, the magnitude of $\dot{Q}_{rev,+}(t)$ increased slightly with increasing current I. By contrast, at the negative electrode [Fig. 7(b)], the reversible heat generation rate $\dot{Q}_{rev,-}(t)$ was both endothermic and exothermic during charging and discharging. The trends observed in $\dot{Q}_{rev,+}(t)$ and $\dot{Q}_{rev,-}(t)$ and their differences were consistent with those observed in EDLC devices with activated carbon electrodes containing carboxymethyl cellulose (CMC) binder [40,41]. There, the behavior of $\dot{Q}_{rev,-}(t)$ was explained by the overscreening effect of ions induced by negatively charged functional groups in CMC binder, as previously discussed [41]. Similarly, in graphene-based electrodes, functional groups such as carboxyl (− COOH) exist and can dissociate to form negatively charged carboxylic (− COO⁻) surface functionalities [61]. The dissociation of − COOH into − COO⁻ is an irreversible spontaneous process that may occur during device assembly or during the first charging/discharging cycle. It could not be observed in the highly repeatable and consecutive cycles shown
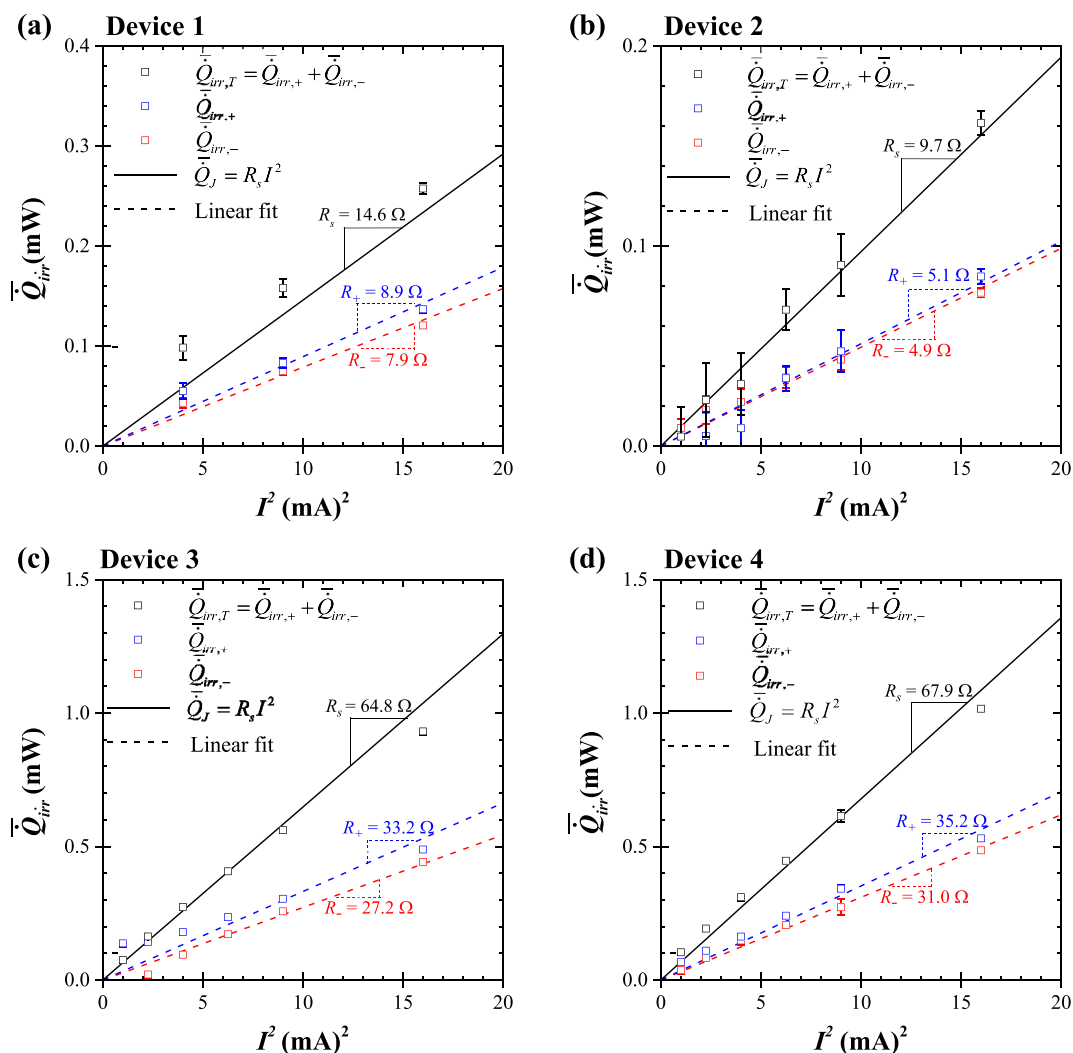
Fig. 6. Time-averaged heat generation rates $\overline{\dot{Q}}_{irr,-}$, $\overline{\dot{Q}}_{irr,+}$, and $\overline{\dot{Q}}_{irr,T}$ under galvanostatic cycling as functions of I^2 for current I ranging between 2 and 4 mA for (a) Device 1, (b) Device 2, (c) Device 3, and (d) Device 4. Heat generation rate $\overline{\dot{Q}}_J = R_s I^2$ due to Joule heating and linear fits of $\overline{\dot{Q}}_{irr,-}$ and $\overline{\dot{Q}}_{irr,+}$ are also shown.

in Fig. 5. The resulting negatively charged functional groups attracted positively charged H^+ cations from H_3PO_4 gel electrolyte via electrostatic force between opposite charge. In order to charge-balance the inner Helmholtz layer in the electrolyte, another sub-sequent layer of PO_4^{3-} anions was required [41,42]. Therefore, at the beginning of the charging step, the negative electrode was first charged by desorption of PO_4^{3-} anion (endothermic) and by H^+ cations adsorption (exothermic) [41,42]. Thus, the endothermic anion desorption present at the electrode/electrolyte interface due to the overscreening effect partially compensated the exothermic cation adsorption during charging at the negative electrode. Therefore, the magnitude of $\dot{Q}_{rev,-}(t)$ was small compared with that of $\dot{Q}_{rev,+}(t)$, at all times. Consequently, the instantaneous reversible heat generation rate in the entire cell $\dot{Q}_{rev,T}(t) = \dot{Q}_{rev,+}(t) + \dot{Q}_{rev,-}(t)$ followed the same trends as $\dot{Q}_{rev,+}(t)$ at all imposed current I [Fig. 7(c)]. At the transition between charging and discharging steps, there was a sight time lag due to response time of the heat flux sensors (0.7 s to reach 95% of actual value, gSKIN-XP, greenTEG) and thermal mass of the GP/BP electrodes and gel electrolyte in Devices 1 and 2.

Finally, Fig. 7(d) plots the time-averaged reversible heat generation over a charging step at each electrode $\overline{Q}_{rev,i}^c$ as a function of current I for Devices 1 and 2. At the negative electrode, $\overline{Q}_{rev,-}^c$ for all currents fell close to 0 mW, indicating a comparable amount of endothermic and exothermic heat generated during a charging step. This result is consistent with $\overline{Q}_{rev,-}^c$ of devices with activated carbon electrodes containing CMC binder reported in Ref. [41]. However, at the positive electrode, $\overline{Q}_{rev,+}^c$ was positive and fairly independent of the imposed current I.

4.5.2. Redox-active gel electrolyte

Fig. 8 shows the instantaneous reversible heat generation rates (a) $\dot{Q}_{rev,+}(t)$ at the positive electrode, (b) $\dot{Q}_{rev,-}(t)$ at the negative electrode, and (c) $\dot{Q}_{rev,T}(t)$ in the entire cell estimated by Equation (7) for Devices 3 and 4 for currents I ranging from 2 to 4 mA. At the positive electrode [Fig. 8(a)], the reversible heat generation rates $\dot{Q}_{rev,+}(t)$ were both endothermic and exothermic during charging and discharging. This can be explained by the combination of two superimposed charging mechanisms at the positive electrode, namely (i) EDL formation and (ii) redox reaction involving $Fe(CN)_6^{3-}$
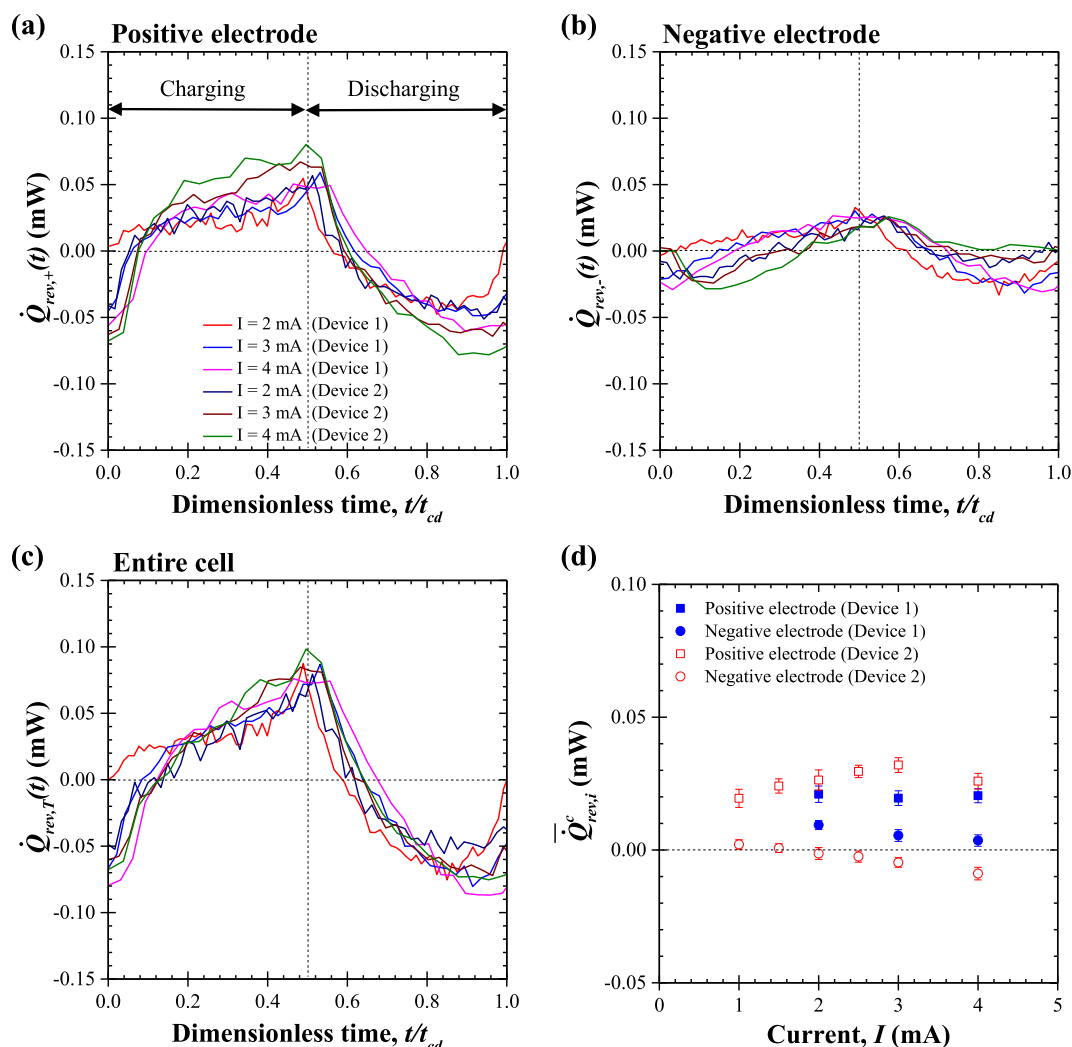
Fig. 7. One charging-discharging cycle of the reversible heat generation rate (a) $\dot{Q}_{rev,+}(t)$ at the positive electrode, (b) $\dot{Q}_{rev,-}(t)$ at the negative electrode, (c) $\dot{Q}_{rev,T}(t)$ in the entire cell for Devices 1 and 2 as functions of dimensionless time t/t_{cd} for constant current $I = 2$, 3, and 4 mA. (d) Corresponding time-averaged reversible heat generation rate $\overline{\dot{Q}}_{rev,+}^c$ at the positive and $\overline{\dot{Q}}_{rev,-}^c$ at the negative electrodes during a charging step for Devices 1 and 2.

and $Fe(CN)_6^{4-}$, as observed in Refs. [62,63]. These two charging mechanisms have opposite thermal signatures: (i) EDL formation/adsorption of $Fe(CN)_6^{3-}$ and $Fe(CN)_6^{4-}$ anions on GP is exothermic and (ii) the oxidation reaction $Fe(CN)_6^{4-} \rightarrow Fe(CN)_6^{3-} + e^-$ in the gel electrolyte was found to be endothermic both experimentally [29,64,65] and analytically, based on entropy considerations [66].

Moreover, in contrast to Devices 1 and 2, the reversible heat generation rate at the negative electrode $\dot{Q}_{rev,-}(t)$ was systematically larger than that at the positive electrode $\dot{Q}_{rev,+}(t)$ for both Devices 3 and 4 at all imposed current I. In addition, the reversible heat generation rates $\dot{Q}_{rev,-}(t)$ were exothermic during charging and endothermic during discharging. Furthermore, the magnitude of $\dot{Q}_{rev,-}(t)$ increased with increasing current I. Note that $\dot{Q}_{rev,-}(t)$ was larger in Device 3 than in Device 4 because the graphene petal mass loading of the negative electrode was about 33% larger in Device 3 than in Device 4 [Fig. 8(b)]. The instantaneous reversible heat generation rate in the entire cell $\dot{Q}_{rev,T}(t) = \dot{Q}_{rev,+}(t) + \dot{Q}_{rev,-}(t)$ followed the behavior observed at the negative electrode for Devices 3 and 4 [Fig. 8(c)]. Here also, there was a slight time lag at the transition between charging and discharging steps,

due to response time of the heat flux sensors (0.7 s to reach 95% of actual value, gSKIN-XP, greenTEG) and thermal mass of the GP/BP electrodes and gel electrolyte in Devices 3 and 4.

Finally, Fig. 8(d) plots the time-averaged reversible heat generation over a charging step at each electrode $\overline{\dot{Q}}_{rev,i}^c$ as a function of current I for Devices 3 and 4. At the positive electrode, $\overline{\dot{Q}}_{rev,+}^c$ was nearly zero for all currents, indicating a comparable amount of endothermic and exothermic heat generated during a charging step. On the other hand, at the negative electrode, $\overline{\dot{Q}}_{rev,-}^c$ in both Devices 3 and 4 was positive and increased with imposed current I. This result is consistent with $\overline{\dot{Q}}_{rev}^c$ at the positive electrodes of EDLC devices consisting of activated carbon electrodes in different electrolytes [40] and that at positive and negative electrodes without CMC binder [41], where neither redox reactions nor overscreening effects were present. Notably, the magnitude of instantaneous reversible heat generation rate $\dot{Q}_{rev,i}(t)$ was larger in Devices 3 and 4 than in Devices 1 and 2 at both electrodes and for any given current I. The value of $\dot{Q}_{rev,+}(t)$, $\dot{Q}_{rev,-}(t)$, and $\dot{Q}_{rev,T}(t)$ in Devices 3 and 4 with redox-active gel electrolyte oscillated between ± 0.2 mW, ± 0.5 mW, and ± 0.7 mW, respectively while
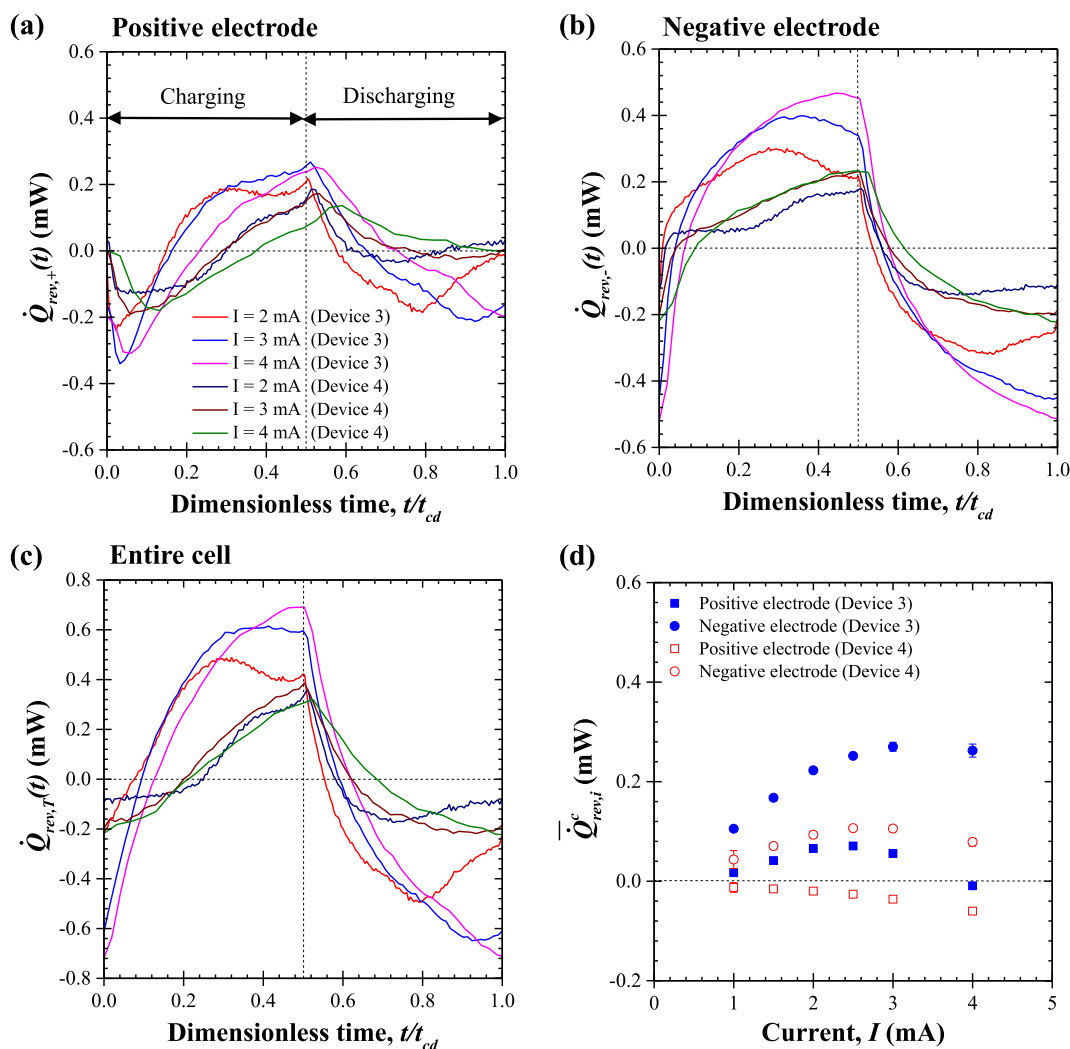
Fig. 8. One charging-discharging cycle of the reversible heat generation rate (a) $\dot{Q}_{rev,+}(t)$ at the positive electrode, (b) $\dot{Q}_{rev,-}(t)$ at the negative electrode, (c) $\dot{Q}_{rev,T}(t)$ in the entire cell for Devices 3 and 4 as functions of dimensionless time t/t_{cd} for constant current $I = 2$, 3, and 4 mA. (d) Corresponding time-averaged reversible heat generation rate $\overline{\dot{Q}}^c_{rev,+}$ at the positive and $\overline{\dot{Q}}^c_{rev,-}$ at the negative electrodes during a charging step for Devices 3 and 4.

$\dot{Q}_{rev,+}(t)$, $\dot{Q}_{rev,-}(t)$, and $\dot{Q}_{rev,T}(t)$ in Devices 1 and 2 with conventional gel electrolyte (without redox reaction) oscillated in a smaller range between $\pm$ 0.05 mW, $\pm$ 0.03 mW, and $\pm$ 0.1 mW, respectively. This could be predominantly attributed to the additional redox reactions that enhance charge storage and led to larger capacitance and thus, stronger thermal signatures. The larger reversible heat generation rate could also be due to the larger potential window for Devices 3 and 4 than those for Devices 1 and 2.

Overall, heat generation in Devices 1 and 2 charged under constant current of 4 mA (see Fig. S4 in Supplementary Materials) would result in a heat flux of up to 2.9 W/m² on each face of the devices representing 3% of the total metabolic heat dissipation rate given off by the body of 91.7 W/m² by convection, radiation and evaporation [67]. On the other hand, the heat generation in Devices 3 and 4 would reach up to 10.7 W/m² representing 12% of the total metabolic heat dissipation rate. Note that the presence of all wearable devices would reduce natural convection and evaporation from the skin. It also remains unclear how the temporal fluctuations in heat generation rate may be perceived by the person wearing such devices. This suggests that active thermal management may be necessary, particularly for devices with redox-active gel electrolytes.

5. Conclusion

This study assesses the effect of gel electrolyte composition on heat generation rate in all-solid-state supercapacitors using graphene petals grown on buckypaper electrodes. Two all-solid-state supercapacitor devices with conventional gel electrolyte (H_3PO_4 in PVA) and other two devices with redox-active gel electrolyte ($K_3Fe(CN)_6$-$K_4Fe(CN)_6$ in PVA) were fabricated and tested for their capacitance, internal resistance, and heat generation rate. For all devices, the measured irreversible heat generation $\overline{Q}_{irr,T}$ was proportional to I^2 and equal to Joule heating $\overline{Q}_J$. It was about five times larger in devices with redox-active gel electrolyte than that in devices with conventional gel electrolyte due to larger internal resistance R_s. Moreover, reversible heat generation rates were different at the positive and negative electrodes of all devices. In a conventional gel electrolyte, at the positive electrode $\dot{Q}_{rev,+}(t)$ was exothermic during charging and endothermic during discharging while at the negative electrode, $\dot{Q}_{rev,-}(t)$ was endothermic at the

beginning of charging step and exothermic for the rest of the charging step due to the effect of overscreening on the charging mechanism. By contrast, at the negative electrode of devices with redox-active gel electrolyte, $\dot{Q}_{rev,-}(t)$ was clearly exothermic during charging and endothermic during discharging whereas $\dot{Q}_{rev,+}(t)$ at the positive electrode combined (i) exothermic EDL formation/adsorption of $Fe(CN)_6^{3-}$ and $Fe(CN)_6^{4-}$ anions on GP and (ii) endothermic redox reaction of $Fe(CN)_6^{4-} \rightarrow Fe(CN)_6^{3-} + e^-$ in the gel electrolyte resulting in both endothermic and exothermic during charging. Overall, heat generation measurements can be used to provide insight into the electrochemical processes occurring during charging/discharging of all-solid-state supercapacitors. They can also be used to design thermal management solutions.

Appendix A. Supplementary data

Supplementary data to this article can be found online at https://doi.org/10.1016/j.electacta.2019.02.031.

References

[1] J.A. Rogers, Electronics for the human body, J. Am. Med. Assoc. 313 (6) (2015) 561—562.
[2] H. Nishide, K. Oyaizu, Toward flexible batteries, Science 319 (5864) (2008) 737—738.
[3] L. Nyholm, G. Nyström, A. Mihranyan, M. Strømme, Toward flexible polymer and paper-based energy storage devices, Adv. Mater. 23 (33) (2011) 3751—3769.
[4] H. Guo, M.-H. Yeh, Y. Zi, Z. Wen, J. Chen, G. Liu, C. Hu, Z.L. Wang, Ultralight cut-paper-based self-charging power unit for self-powered portable electronic and medical systems, ACS Nano 11 (5) (2017) 4475—4482.
[5] F. Meng, Y. Ding, Sub-micrometer-thick all-solid-state supercapacitors with high power and energy densities, Adv. Mater. 23 (35) (2011) 4098—4102.
[6] W. Liu, C. Lu, H. Li, R.Y. Tay, L. Sun, X. Wang, W.L. Chow, X. Wang, B.K. Tay, Z. Chen, J. Yan, K. Feng, G. Lui, R. Tjandra, L. Rasenthiram, G. Chui, A. Yu, Paper-based all-solid-state flexible micro-supercapacitors with ultra-high rate and rapid frequency response capabilities, J. Mater. Chem. 4 (10) (2016) 3754—3764.
[7] A. Ramadoss, K.-Y. Yoon, M.-J. Kwak, S.-I. Kim, S.-T. Ryu, J.-H. Jang, Fully flexible, lightweight, high performance all-solid-state supercapacitor based on 3-Dimensional-graphene/graphite-paper, J. Power Sources 337 (2017) 159—165.
[8] L. Yuan, X.-H. Lu, X. Xiao, T. Zhai, J. Dai, F. Zhang, B. Hu, X. Wang, L. Gong, J. Chen, C. Hu, Y. Tong, J. Zhou, Z.L. Wang, Flexible solid-state supercapacitors based on carbon nanoparticles/MnO₂ nanorods hybrid structure, ACS Nano 6 (1) (2011) 656—661.
[9] Y.J. Kang, H. Chung, C.-H. Han, W. Kim, All-solid-state flexible supercapacitors based on papers coated with carbon nanotubes and ionic-liquid-based gel electrolytes, Nanotechnology 23 (6) (2012), 065401.
[10] Y. Xie, Y. Liu, Y. Zhao, Y.H. Tsang, S.P. Lau, H. Huang, Y. Chai, Stretchable all-solid-state supercapacitor with wavy shaped polyaniline/graphene electrode, J. Mater. Chem. 2 (24) (2014) 9142—9149.
[11] Z.-S. Wu, D.-W. Wang, W. Ren, J. Zhao, G. Zhou, F. Li, H.-M. Cheng, Anchoring hydrous RuO₂ on graphene sheets for high-performance electrochemical capacitors, Adv. Funct. Mater. 20 (20) (2010) 3595—3602.
[12] J.Y. Hwang, M.F. El-Kady, Y. Wang, L. Wang, Y. Shao, K. Marsh, J.M. Ko, R.B. Kaner, Direct preparation and processing of graphene/RuO₂ nanocomposite electrodes for high-performance capacitive energy storage, Nano Energy 18 (2015) 57—70.
[13] S. Chen, J. Zhu, X. Wu, Q. Han, X. Wang, Graphene oxide- MnO₂ nanocomposites for supercapacitors, ACS Nano 4 (5) (2010) 2822—2830.
[14] N. Li, J, Wang, Y. Zhao, Y. Ding, L. Guan, MnO₂ nanoflakes coated on multi-walled carbon nanotubes for rechargeable lithium-air batteries, Electrochem. Commun. 13 (7) (2011) 698—700.
[15] K.R. Prasad, N. Munichandraiah, Fabrication and evaluation of 450 F electrochemical redox supercapacitors using inexpensive and high-performance, polyaniline coated, stainless-steel electrodes, J. Power Sources 112 (2) (2002) 443—451.
[16] D.-W. Wang, F. Li, J. Zhao, W. Ren, Z.-G. Chen, J. Tan, Z.-S. Wu, I. Gentle, G.Q. Lu, H.-M. Cheng, Fabrication of graphene/polyaniline composite paper via in situ anodic electropolymerization for high-performance flexible electrode, ACS Nano 3 (7) (2009) 1745—1752.
[17] K. Jurewicz, S. Delpeux, V. Bertagna, F. Beguin, E. Frackowiak, Supercapacitors from nanotubes/polypyrrole composites, Chem. Phys. Lett. 347 (1—3) (2001) 36—40.
[18] P.A. Mini, A. Balakrishnan, S.V. Nair, K.R.V. Subramanian, Highly super capacitive electrodes made of graphene/poly(pyrrole), Chem. Commun. 47

[19] B. Akinwolemiwa, C. Peng, G.Z. Chen, Redox electrolytes in supercapacitors, J. Electrochem. Soc. 162 (5) (2015) A5054—A5059.
[20] S.T. Senthilkumar, R.K. Selvan, J.S. Melo, Redox additive/active electrolytes: a novel approach to enhance the performance of supercapacitors, J. Mater. Chem. 1 (40) (2013) 12386—12394.
[21] H. Yu, J. Wu, L. Fan, K. Xu, X. Zhong, Y. Lin, J. Lin, Improvement of the performance for quasi-solid-state supercapacitor by using PVA—KOH—KI polymer gel electrolyte, Electrochim. Acta 56 (20) (2011) 6881—6886.
[22] A. Singh, A. Chandra, Enhancing specific energy and power in asymmetric supercapacitors - a synergetic strategy based on the use of redox additive electrolytes, Sci. Rep. 6 (2016) 25793.
[23] G. Ma, J. Li, K. Sun, H. Peng, J. Mu, Z. Lei, High performance solid-state supercapacitor with PVA—KOH—K₃[Fe(CN)₆] gel polymer as electrolyte and separator, J. Power Sources 256 (2014) 281—287.
[24] K. Chen, F. Liu, D. Xue, S. Komarneni, Carbon with ultrahigh capacitance when graphene paper meets K₃Fe(CN)₆, Nanoscale 7 (2) (2015) 432—439.
[25] K. Sun, E. Feng, H. Peng, G. Ma, Y. Wu, H. Wang, Z. Lei, A simple and high-performance supercapacitor based on nitrogen-doped porous carbon in redox-mediated sodium molybdate electrolyte, Electrochim. Acta 158 (2015) 361—367.
[26] S.T. Senthilkumar, R.K. Selvan, J.S. Melo, C. Sanjeeviraja, High performance solid-state electric double layer capacitor from redox mediated gel polymer electrolyte and renewable tamarind fruit shell derived porous carbon, ACS Appl. Mater. Interfaces 5 (21) (2013) 10541—10550.
[27] J. Zhong, L.-Q. Fan, X. Wu, J.-H. Wu, G.-J. Liu, J.-M. Lin, M.-L. Huang, Y.-L. Wei, Improved energy density of quasi-solid-state supercapacitors using sandwich-type redox-active gel polymer electrolytes, Electrochim. Acta 166 (2015) 150—156.
[28] G. Wang, R. Liang, L. Liu, B. Zhong, Improving the specific capacitance of carbon nanotubes-based supercapacitors by combining introducing functional groups on carbon nanotubes with using redox-active electrolyte, Electrochim. Acta 115 (2014) 183—188.
[29] T. Ozeki, I. Watanbe, S. Ikeda, Study of the Prussian blue/Prussian white redox reaction by cyclic voltammothermometry, J. Electroanal. Chem. Interfacial Electrochem. 236 (1—2) (1987) 209—218.
[30] P. Guillemet, Y. Scudeller, T. Brousse, Multi-level reduced-order thermal modeling of electrochemical capacitors, J. Power Sources 157 (1) (2006) 630—640.
[31] H. Gualous, H. Louahlia-Gualous, R. Gallay, A. Miraoui, Supercapacitor thermal modeling and characterization in transient state for industrial applications, IEEE Trans. Ind. Appl. 45 (3) (2009) 1035—1044.
[32] M. Al Sakka, H. Gualous, J. Van Mierlo, H. Culcu, Thermal modeling and heat management of supercapacitor modules for vehicle applications, J. Power Sources 194 (2) (2009) 581—587.
[33] X. Xu, B.G. Sammakia, B.T. Murray, D. Jung, T. Eilertsen, Thermal modeling and heat management of supercapacitor modules by high velocity impinging fan flow, in: ASME 2011 International Mechanical Engineering Congress and Exposition, vol. 10, American Society of Mechanical Engineers, Denver, Colorado, 2011, pp. 1029—1037, 11.
[34] J. Schiffer, D. Linzen, D.U. Sauer, Heat generation in double layer capacitors, J. Power Sources 160 (1) (2006) 765—772.
[35] A.L. d'Entremont, L. Pilon, First-order thermal model of commercial EDLCs, Appl. Therm. Eng. 67 (12) (2014) 439—446.
[36] A.L. d'Entremont, L. Pilon, First-principles thermal modeling of electric double layer capacitors under constant-current cycling, J. Power Sources 246 (2014) 887—898.
[37] A.L. d'Entremont, L. Pilon, Thermal effects of asymmetric electrolytes in electric double layer capacitors, J. Power Sources 273 (2015) 196—209.
[38] A.L. d'Entremont, L. Pilon, First-principles thermal modeling of hybrid pseudocapacitors under galvanostatic cycling, J. Power Sources 335 (2016) 172—188.
[39] Y. Dandeville, P. Guillemet, Y. Scudeller, O. Crosnier, L. Athouel, T. Brousse, Measuring time-dependent heat profiles of aqueous electrochemical capacitors under cycling, Thermochim. Acta 526 (1—2) (2011) 1—8.
[40] O. Munteshari, J. Lau, A. Krishnan, B. Dunn, L. Pilon, Isothermal calorimeter for measurements of time-dependent heat generation rate in individual supercapacitor electrodes, J. Power Sources 374 (2018) 257—268.
[41] O. Munteshari, J. Lau, D.S. Ashby, B. Dunn, L. Pilon, Effects of constituent materials on heat generation in individual EDLC electrodes, J. Electrochem. Soc. 165 (7) (2018) A1547—A1557.
[42] M.Z. Bazant, B.D. Storey, A.A. Kornyshev, Double layer in ionic liquids: overscreening versus crowding, Phys. Rev. Lett. 106 (4) (2011), 046102.
[43] M.D. Levi, N. Levy, S. Sigalov, G. Salitra, D. Aurbach, J. Maier, Electrochemical quartz crystal microbalance EQCM studies of ions and solvents insertion into highly porous activated carbons, J. Am. Chem. Soc. 132 (38) (2010) 13220—13222.
[44] T. Bhuvana, A. Kumar, A. Sood, R.H. Gerzeski, J. Hu, V.S. Bhadram, C. Narayana, T.S. Fisher, Contiguous petal-like carbon nanosheet outgrowths from graphite fibers by plasma CVD, ACS Appl. Mater. Interfaces 2 (3) (2010) 644—648.
[45] G. Xiong, K.P.S.S. Hembram, R.G. Reifenberger, T.S. Fisher, MnO₂-coated graphitic petals for supercapacitor electrodes, J. Power Sources 227 (2013) 254—259.
[46] G. Xiong, C. Meng, R.G. Reifenberger, P.P. Irazoqui, T.S. Fisher, Graphitic petal electrodes for all-solid-state flexible supercapacitors, Adv. Energy Mater. 4 (3)

(2014) 1300515.

[47] L. Pilon, H. Wang, A.L. d'Entremont, Recent advances in continuum modeling of interfacial and transport phenomena in electric double layer capacitors, J. Electrochem. Soc. 162 (5) (2015) A5158–A5178.

[48] A. Burke, M. Miller, Testing of electrochemical capacitors: capacitance, resistance, energy density, and power capability, Electrochim. Acta 55 (25) (2010) 7538–7548.

[49] S. Zhao, F. Wu, L. Yang, L. Gao, A.F. Burke, A measurement method for determination of dc internal resistance of batteries and supercapacitors, Electrochem. Commun. 12 (2) (2010) 242–245.

[50] M.D. Stoller, R.S. Ruoff, "Best practice methods for determining an electrode material's performance for ultracapacitors", Energy Environ. Sci. 3 (9) (2010) 1294–1301.

[51] B.-A. Mei, O. Munteshari, J. Lau, B. Dunn, L. Pilon, Physical interpretations of nyquist plots for EDLC electrodes and devices, J. Phys. Chem. C 122 (1) (2017) 194–206.

[52] H.-L. Girard, H. Wang, A.L. dEntremont, L. Pilon, Physical interpretation of cyclic voltammetry for hybrid pseudocapacitors, J. Phys. Chem. C 119 (21) (2015) 11349–11361.

[53] H. Yoon, H.-J. Kim, J.J. Yoo, C.-Y. Yoo, J.H. Park, Y.A. Lee, W.K. Cho, Y.-K. Han, D.H. Kim, Pseudocapacitive slurry electrodes using redox-active quinone for high-performance flow capacitors: an atomic-level understanding of pore texture and capacitance enhancement, J. Mater. Chem. 3 (46) (2015) 23323–23332.

[54] Y. Liu, B. Weng, J.M. Razal, Q. Xu, C. Zhao, Y. Hou, S. Seyedin, R. Jalili, G.G. Wallace, J. Chen, High-performance flexible all-solid-state supercapacitor from large free-standing graphene-PEDOT/PSS films, Sci. Rep. 5 (2015) 17045.

[55] G. Wang, H. Wang, X. Lu, Y. Ling, M. Yu, T. Zhai, Y. Tong, Y. Li, Solid-state supercapacitor based on activated carbon cloths exhibits excellent rate capability, Adv. Mater. 26 (17) (2014) 2676–2682.

[56] A.J. Bard, L.R. Faulkner, Electrochemical Methods: Fundamentals and Applications, John Wiley & Sons, New York, NY, 2001.

[57] A.L. d'Entremont, H.-L. Girard, H. Wang, L. Pilon, Electrochemical transport phenomena in hybrid pseudocapacitors under galvanostatic cycling, J. Electrochem. Soc. 163 (2) (2016) A229–A243.

[58] P. Yang, K. Liu, Q. Chen, X. Mo, Y. Zhou, S. Li, G. Feng, J. Zhou, Wearable thermocells based on gel electrolytes for the utilization of body heat, Angew. Chem. Int. Ed. 55 (39) (2016) 12050–12053.

[59] A. Kundu, T.S. Fisher, Harnessing the thermogalvanic effect of the ferro/ferricyanide redox couple in a thermally chargeable supercapacitor, Electrochim. Acta 281 (2018) 357–369.

[60] K.K. Lian, C. Li, R.H. Jung, J.G. Kincs, Electrochemical cell having symmetric inorganic electrodes, US Patent 5 (587) (1996) 872. Dec. 24.

[61] M. Elimelech, W.H. Chen, J.J. Waypa, Measuring the zeta (electrokinetic) potential of reverse osmosis membranes by a streaming potential analyzer, Desalination 95 (3) (1994) 269–286.

[62] Y. Tian, J. Yan, R. Xue, B. Yi, Capacitive properties of activated carbon in $K_4Fe(CN)_6$, J. Electrochem. Soc. 158 (7) (2011) A818–A821.

[63] J. Lee, S. Choudhury, D. Weingarth, D. Kim, V. Presser, High performance hybrid energy storage with potassium ferricyanide redox electrolyte, ACS Appl. Mater. Interfaces 8 (36) (2016) 23676–23687.

[64] B. Korth, T. Maskow, C. Picioreanu, F. Harnisch, The microbial electrochemical peltier heat: an energetic burden and engineering chance for primary microbial electrochemical technologies, Energy Environ. Sci. 9 (8) (2016) 2539–2544.

[65] P. Boudeville, A. Tallec, Electrochemistry and calorimetry coupling: IV. determination of electrochemical peltier heat, Thermochim. Acta 126 (1988) 221–234.

[66] Y. Maeda, T. Kumagai, Electrochemical peltier heat in the polypyrrole-electrolyte system, Thermochim. Acta 267 (1995) 139–148.

[67] S. Murakami, S. Kato, J. Zeng, Combined simulation of airflow, radiation and moisture transport for heat release from a human body, Build. Environ. 35 (6) (2000) 489–500.